Photonic Processing of MAPbI₃ Films by Flash Annealing and Rapid Growth for High-Performance Perovskite Solar Cells

Patricio Serafini, Pablo P. Boix, Eva M. Barea, Tomas Edvinson, Sandy Sánchez, and Iván Mora-Seró*

Defects in polycrystalline halide perovskite films can cause a decrease of the solar cell photoconversion efficiency and stability. The perovskite film enhanced during crystal growth by controlling the processing method can alleviate defects and the related recombination sites that affect the performance of cells. Herein, flash infrared annealing is employed to crystallize methylammonium lead iodide perovskite with a single heating pulse, where uniform grain domains are optically observed and mapped. Films are annealed with different temperature ramps up to $48\,°C\,s^{-1}$ heating rate. Annealing with higher heating rates presents lower defect densities, decreases the Urbach energy tail, and improves the optoelectrical performance of the films. These improvements are rationalized by Raman spectroscopy of nucleation points and grain surface differences among the process variations. The role of crystal growth and subsequent film quality allows to achieve a champion photovoltaic device growth at $48\,°C\,s^{-1}$ with stability around 250 h under 1 sun illumination and 60% relative humidity for 100 h under 3 sun (AM1.5G) illumination. In situ optical imaging is recorded during the process, confirming that rapid annealing, i.e., higher heating rates, contributes to obtain more stable devices with the added advantage of shorter processing time.

1. Introduction

Halide perovskites (HPs) were applied as light absorbing material in solar cells for the first time in 2009 yielding power conversion efficiency (PCE) of 3.8%.[1] Nowadays, the efforts of many research groups have skyrocketed this figure to values above 25%,[2] making HPs serious candidates to compete and complement well-established photovoltaic technologies such as silicon solar cells.[3–6] The path to high efficiency in devices of societal use requires both film deposition optimization and device engineering compatible with industrial routes for final commercialization. When focusing mainly on the photoactive layer, where charge carriers are produced, approaches to reduce the defect concentration have included crystal growth control, posttreatments, and interfacial modifications.[7–9] Defects in perovskite are susceptible to film deposition conditions[10,11] which can lead to an unbalanced stoichiometry at the grains surface resulting in decomposition of organic molecules during thermal annealing process.[12–14] The latter provides routes to form defect states, provoking surface recombination[15] via shallow or deep trap states.[16–18] In line with this, photoluminescence (PL) at grain boundaries often show lower intensities compared to grain interiors, indicating more defects and a faster nonradiative recombination.[19] Also, defects at grain boundaries

P. Serafini, E. M. Barea, I. Mora-Seró
Institute of Advanced Materials (INAM)
Universitat Jaume I
12071 Castelló de la Plana, Spain
E-mail: sero@uji.es

P. P. Boix
Instituto de Ciencia de los Materiales (ICMUV)
Universitat de Valencia
46980 Paterna, Spain

T. Edvinson
Department of Materials Science and Engineering
Ångström Laboratory
Uppsala University
SE-75237 Uppsala, Sweden

S. Sánchez
Laboratory for Molecular Engineering of Optoelectronic Nanomaterials
Institute of Chemistry and Chemical Engineering
École Polytechnique Fédérale de Lausanne
1015 Lausanne, Switzerland

S. Sánchez
Laboratory of Photonics and Interfaces
Institute of Chemistry and Chemical Engineering
École Polytechnique Fédérale de Lausanne
1015 Lausanne, Switzerland

are vulnerable for degradation as they provide charge accumulation sites and infiltration pathway of water vapor.[20] According to this, it has been shown that HP materials degrade along these sites when both moisture and trapped charges exist simultaneously.[20] Particularly, the presence of water molecules which are known to form hydrates[21,22] allowing charges trapped at the defect site to easily deteriorate the HPs structure. In addition, the aforementioned sites are considered as one of the main reasons for the appearance of hysteresis as defects could provide a favorable pathway for ion migration due to reduced steric hindrance.[23,24]

One approach used to control defects in HP films without altering the perovskite chemistry is based on the grain size enlargement. In polycrystalline materials, including HP films, grain size is highly related to crystallization rate during the film formation.[25–27] Different processing procedures such as one-step deposition, antisolvent method, and two-step deposition method are widely used to tune and adjust the film formation. These techniques can result in films with fewer defects and large (order of micrometers) compact grains result in lower trap state density and reduced recombination centers.[24,28] Therefore, a promising and viable route to produce high-quality HPs by controlling perovskite growth, which influences in defect control, will yield to high-efficiency and long-term stability.[29–31]

At laboratory scale, the most extensively used technique to produce perovskite film is the antisolvent method followed by the annealing of films. The antisolvent-assisted crystallization lowers the precursor solubility giving rise to supersaturation where nucleation points arise and trigger further crystal growth. Afterward, an annealing step removes the remaining solvent and aids to the final phase transformation of the perovskite film.[32] It has been shown that if the antisolvent technique is used in an optimized fashion, the resulting films are compact with a smooth surface with relatively few defects, enabling high efficiency on the manufactured devices. However, the antisolvent approach is so far restricted to spin coating deposition on small-area devices and difficult to implement in other deposition methods that are compatible with upscaling. The approach is also highly procedure dependent where several parameters must be optimized to achieve an optimal reproducible device, such as the antisolvent application (timing, quantity, and type of solvent), largely depending on the skills of the individual device manufacturer.

For future implementation of HPs at industrial scale, a process to fabricate low defect films in large areas with negligible environmental impact will be required. In this context, an extension of an antisolvent step to enforce proper crystallization of HP films cannot be easily transferred to large substrates.[33–35] On the other hand, a technique, such as flash infrared annealing (FIRA),[36–39] has shown in last years performance in the same range of devices prepared with the antisolvent method. In addition, the mentioned technique has shown the possibility of synthesized perovskite films in big areas of 100 cm^2,[37] yet avoiding the antisolvent step. In addition, the environmental impacts of FIRA are less than 10% of those produced in fabricating using the antisolvent methodology as previously reported.[40]

FIRA equipment consists of a closed chamber with cold water circulation that keeps temperature around 10 °C. Inside the equipment there are O_2 and N_2 flows to fill the ambient where the substrate with perovskite is placed. Finally, there are six IR lamps that controlled by a software that sets the time and power conditions of the light pulse[41,42] While final temperature of the annealing plays a role, even a more important role is the annealing time defined by the temperature ramp. In this work, we have systematically analyzed the effect of heating rates in the HPs crystallization process in FIRA-processed films and their implications for the final photovoltaic devices' performance and stability.

We use MAPbI$_3$ due to the characteristics as high charge carrier mobility,[43] with low binding energy, optimal bandgap around[44] 1.6 eV accompanied by effective radiative recombination[45] of charge carriers, but can be extended to other HPs in a later stage. In addition, as a proof-of-concept this material has been proven to be optimal for FIRA processing and the manufactured devices, achieving high efficient PSCs.[37,46]

The maximum temperature reached by FIRA of 120 °C was selected as the temperature of crystallization that leads to high-performance efficiency.[47–50] Controlling the temperature increase per unit of time, the annealing rate, we analyze the perovskite crystallization and its repercussion on efficiency and stability by employing FIRA technique. In particular, the differences between the perovskite films and their effect on the degradation mechanism were analyzed from their microscale zone characteristics. FIRA process allows the growth of a compact film, resulting in the formation of micrometric scale domains. These domains are composed of many grains with defined growth orientation and same internal structure, characterized by a nucleation center point with defined borders appreciable at micrometer scale which enables optical microscope observations[49,51–54] and micrometer resolved Raman spectroscopy and PL. Thus, this work establish the correlation between annealing rates and intrinsic film quality and stability by measuring chronoamperometry and optical absorbance over time while we observe the film surface change by optical image acquisition in transmission mode. This analysis presents a physical correlation of optoelectronic performance with microscopically observable chemical surface changes.

2. Results and Discussion

In order to fabricate MAPbI$_3$ films, solutions containing perovskite precursors were deposited on glass/FTO/compact TiO$_2$/mesoporous TiO$_2$ substrates, see Experimental Section for further details. After the solution deposition process, solvent evaporation and MAPbI$_3$ crystallization were achieved using the FIRA process. A photonic pulse raises the chamber temperature to 120 °C, with a heating rate of 21.3 °C s^{-1}, and results in complete film coverage of the surface thanks to an optimum equilibrium between nucleation and crystal growth. The photonic pulse result in compact grains domains of 50 μm of diameter average as shown in **Figure 1**a. The surface temperature measured by a pyrometer sensor (see methods) can be seen in Figure 1, and reflects the perovskite films low thermal conductivity.[55–57] The use of shorter heating rates, i.e., longer pulse times, leads to large and nonhomogeneous dendrites formation due to different and lower tips growth velocity.[10,58]
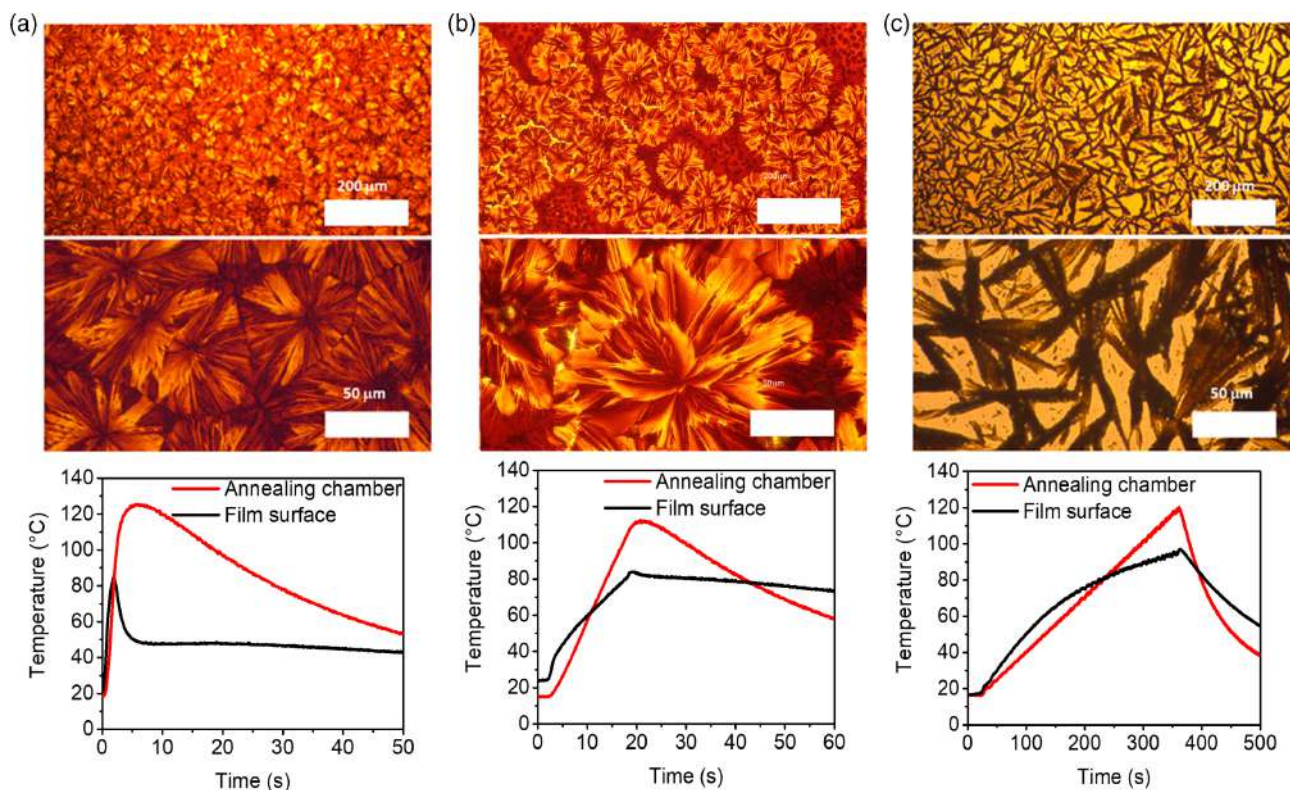
Figure 1. Optical images in transmission mode and its temperature profile for MAPbI$_3$ IR annealed wet films; a) 21.3 °C s^{-1}, b) 5 °C s^{-1}, and c) 0.29 °C s^{-1}.

To corroborate the uniformity in surface observed by the optical microscope, surface electron microscopy (SEM) images were taken on the films prepared with 48 and 29 °C s^{-1} heating rates (**Figure 2**a) and the remaining used pulses (Figure S2, Supporting Information). From this, it was possible to observe that 48 °C s^{-1} resulted in larger and compact grains while 29.4 °C s^{-1} exhibits smaller crystal grains, indicating that higher heating rate contributes to a better grain growth, ultimately beneficial for higher quality films and better devices performance. The short duration of the flash corresponding to higher heating rates makes the system especially interesting for industrial applications.[40]

Raman spectra were measured in two different regions of the grain domain, one is the nucleation center and the other is over the surface of the grain domain, for samples annealed at 29.4 and 5 °C s^{-1} (see Figure S1a,b, Supporting Information, respectively). The 29.4 °C s^{-1} annealing shows typical Raman spectra of MAPbI$_3$ perovskite phase,[59] with reflections at 69, 94, and 108 cm^{-1} in the nucleation point as well as in the grain domain indicating the conservation of phase along the grain. Though, at lower heating rate, 5 °C s^{-1}, reflection points of MAPbI$_3$ perovskite phase are only observed at the center of the nucleation-point, but not in outer regions correspondence to the grain (Figure S1b, Supporting Information), showing no evidence of the tetragonal perovskite phase but mainly to PbX$_6$ sublattice modes.[60–63]

In addition, photothermal deflection spectroscopy (PDS) was used to measure the layer light absorption with high sensibility, in order to study the impact of heating rate on the formation of perovskite crystals with fewer defects. As shown in Figure S1c, Supporting Information, the PDS spectrum reflects how absorption sharply decreases at lower heating rates, i.e., 5 and 0.29 °C s^{-1} while there is a slight difference between 48 and 29.4 °C s^{-1}. The results of this characterization are summarized in **Table 1**, showing an inverse relation between heating rate and Urbach energy tail for the processed perovskite films.[64,65] Upon the small difference in the heating rate between the samples obtained at 48 and 29.4 °C s^{-1}, the Urbach energy still decreases as the structure could have fewer vacancies in terms of defects and a more ordered crystal structure.

In accordance with lower defected density extrapolated from the PDS characterization, UV–vis absorption at Figure 2b exhibits higher intensity for the films prepared with 48 °C s^{-1} in comparison to 29.4 °C s^{-1}, while the remaining films exposed lower or negligible intensities, (Figure S3, Supporting Information). The photoluminescence (PL) intensities for 48 °C s^{-1} films were higher than 29.4 °C s^{-1} films and significantly higher than the ones observed for 5 and 0.29 °C s^{-1}, films are displayed in Figure 2c, pointing to a clear decrease of nonradiative recombination. In addition, time-resolved PL (TRPL) measurements were performed (Figure 2c) to analyze the lifetime of charge carriers (τ). The results signified by the single exponential decay give a lower slope ($m = -1/\tau$) for higher heating rate confirming the decrease of nonradiative recombination. These results point out that the higher annealing rate produces better film quality with lower defects that improves absorbance and inhibit the recombination, compared lower annealing rates.
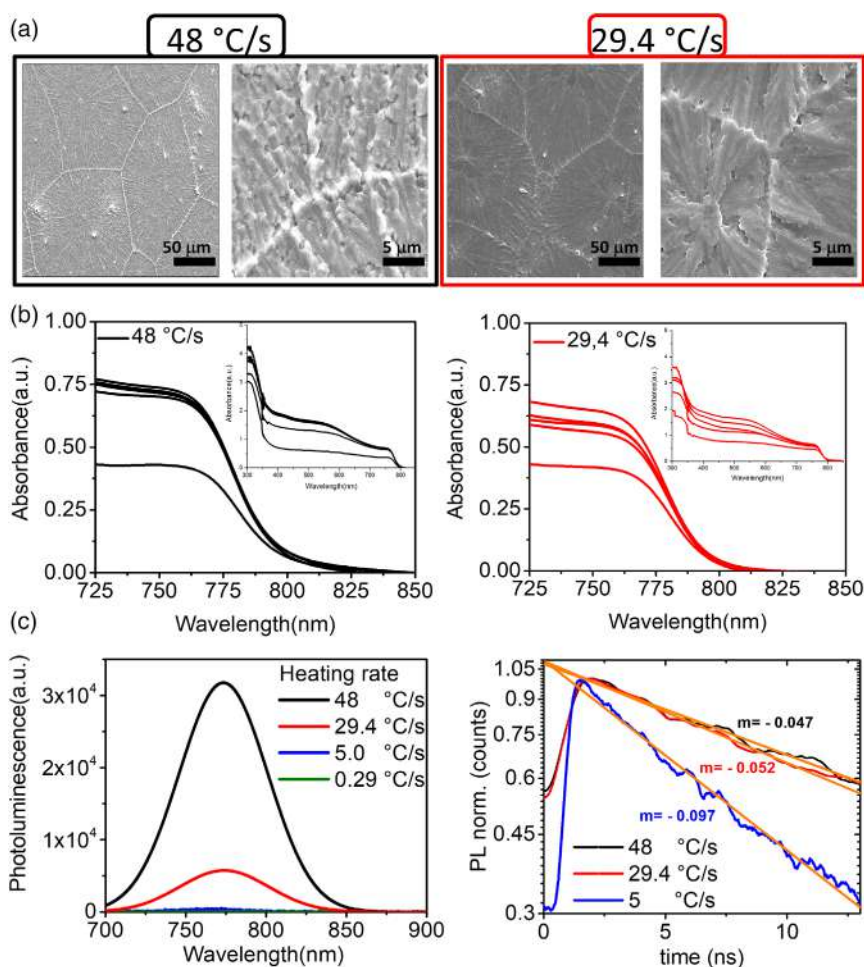
Figure 2. a) SEM of perovskite surface annealed at different times measured at 500× magnification (left) and 5000× magnification (right). b) Absorbance measurement at different spots of surface films annealed at 48 and 29.4 °C s^{-1}. c) PL measurement at different annealed times and TRPL of films at different annealing time.

Table 1. Urbach energy values of different heating rate.

Annealing time [s]	Temperature rate [°C s^{-1}]	Urbach energy [MeV]
1	48	20.43
1.6	29.4	21.78
18	5	179.78
360	0.59	193.89

Confocal microscopy (CM) showed smoother and more uniform surfaces for the 48 °C s^{-1} films reflected from standard deviation values (Figure S4a, Supporting Information). In contrast, films annealed at 29.4 °C s^{-1} exhibited rougher areas with the presence of holes or defects (Figure S4b, Supporting Information). The same behavior was observed when vertical approach measurements were performed (Figure S4c, Supporting Information), with more uniform PL intensities for higher annealing rate contrary to lower annealing rate were defects of different depth contributes.

Atomic force microscopy (AFM) measurements in areas of 50 and 5 μm^2 (see Figure S5, Supporting Information) were employed to analyze surface roughness. The line profiles of measurement for both areas of the 48 and 29.4 °C s^{-1} films showed similar trends of hills and peaks variations with lower presence of them in 48 °C s^{-1} sample. The latter was also apparent in the indexed table with statistically extracted parameters such as average roughness (R_a) and root mean square roughness (R_q), pointing to smoother surface for 48 °C s^{-1} films in each analyzed area.

Perovskite solar cells were fabricated with the HP films with most promising optoelectronic quality and film morphology (the films annealed with 48 and 29.4 °C s^{-1} heating rates). Devices were prepared in a structure of glass/FTO/TiO$_2$ (compact layer)/TiO$_2$-mesoporous/MAPbI$_3$/Spiro/Au according to the Experimental Section. The different parameters obtained by measuring under 1 sun illumination for 48 and 29.4 °C s^{-1} are plotted in **Figure 3**a. Devices prepared with a perovskite layer using 48 °C s^{-1} heating rate presented an average photoconversion efficiency (PCE) higher than samples prepared with 29.4 °C s^{-1} heating rate (see Figure 3a). Apart from one outlier device, higher and significantly less spread values in V_{oc} and J_{sc} can be seen for the samples with 48 °C s^{-1} heating rate compared to the 29.4 °C s^{-1} heating rate devices.
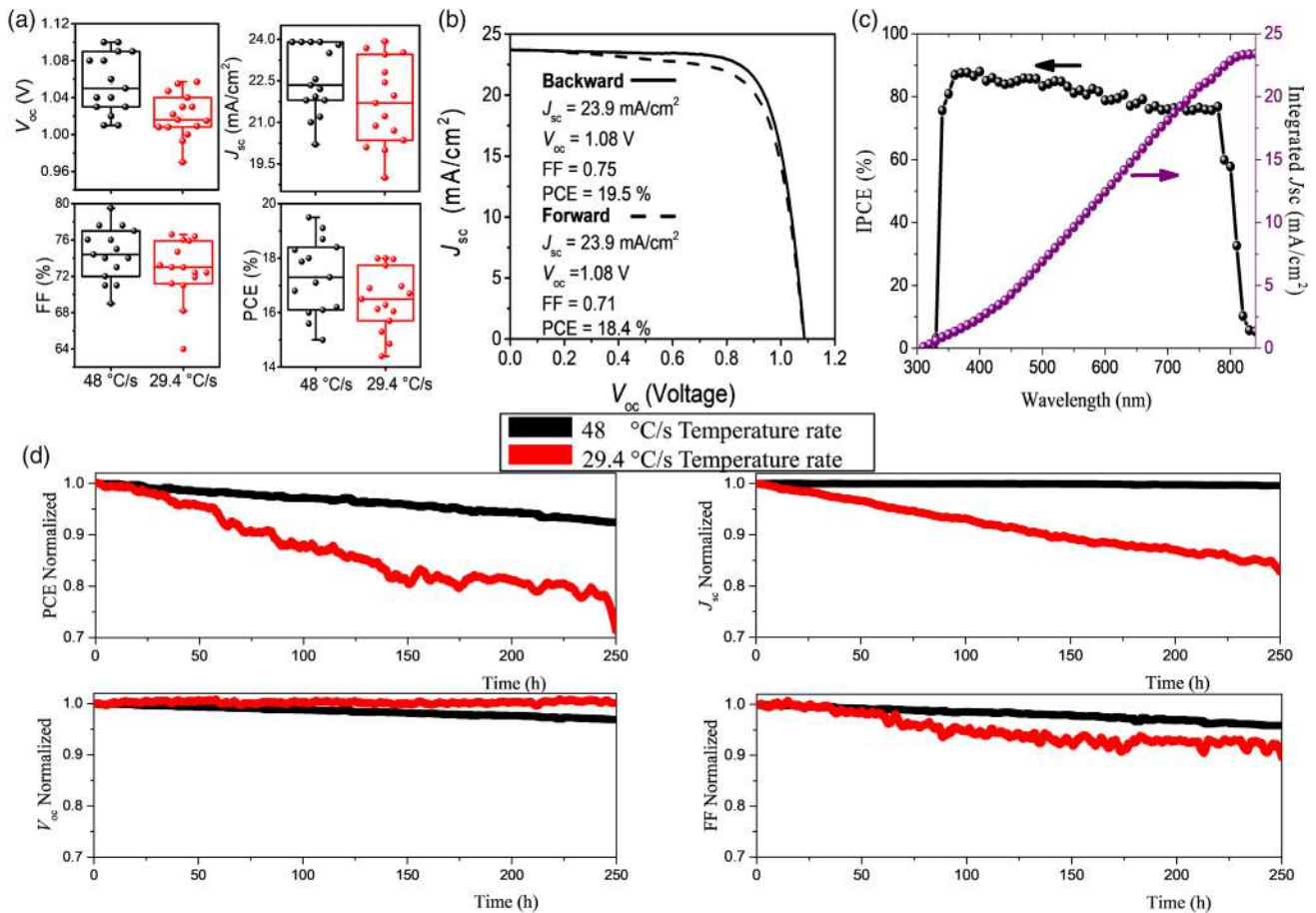
Figure 3. a) Statistical values of PV parameters measured in the solar simulator at 48 and 29.4 °C s^{-1} heating rates. b) J–V curve of record device obtained at 48 °C s^{-1}. c) IPCE measurement of record device. d) Samples parameters tested for stability measured continuously under 1 sun illumination with nitrogen flow.

The increase of PCE is due mainly to an enhancement of open-circuit potential, V_{oc}, and short-circuit current, J_{sc}, that compensates the higher average fill factor, FF, observed for samples prepared with 29.4 °C s^{-1} heating rate. These improvements are attributed to the larger grains dimensions with less defect concentration, reducing the nonradiative recombination as previously commented.[66–68] J–V curves and photovoltaic

parameters of champion devices prepared with 48 °C s^{-1} heating rate are plotted in Figure 3b. The device shows $J_{sc} = 23.9$ mA cm^{-2}, $V_{oc} = 1.08$ V, FF = 0.75 and a resulting PCE of 19.5% in the backward scan. Furthermore, the device exhibits low J–V curve hysteresis but a drop in the FF from 0.75 to 0.71 and a forward-scan PCE of 18.4% (average PCE 18.95%). To verify the J_{sc} obtained, incident photon-to-electron
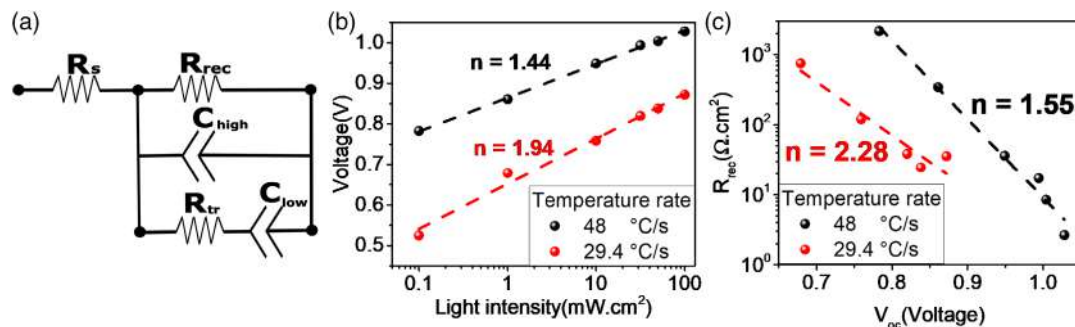

Figure 4. a) Equivalent circuit model employed with impedance spectroscopy analysis.[69] b) Voc vs Light intensity. c) Recombination resistances over at different voltages. The n values (recombination behavior) are calculated from the slope of the straight lines.

efficiency (IPCE) was measured observing in a similar J_{sc} (see Figure 3c).

The stability of the devices was systematically characterized under nitrogen flow with 1 sun illumination at maximum power point (MPP) (see Experimental Section for further details). The evolution of the photovoltaic parameters is shown in Figure 3d. Interestingly, V_{oc} remains practically constant while J_{sc} and FF display clearer degradation particularly for the $29.4\,°C\,s^{-1}$ samples, consequently resulting in a greater PCE stability for $48\,°C\,s^{-1}$.

The devices were characterized using electrochemical impedance spectroscopy (EIS) to learn more about how the different heating rate affect the electronic behavior. EIS spectra were fitted using the equivalent circuit depicted in **Figure 4**a.[69] The circuit consists of a series resistance (R_s) in series with the parallel association of three branches. Recombination resistance, R_{rec}, can be considered negligible compared to the transport resistance in a good quality HP layer[69] in parallel with a high-frequency geometrical capacitance, C_g, and a low-frequency
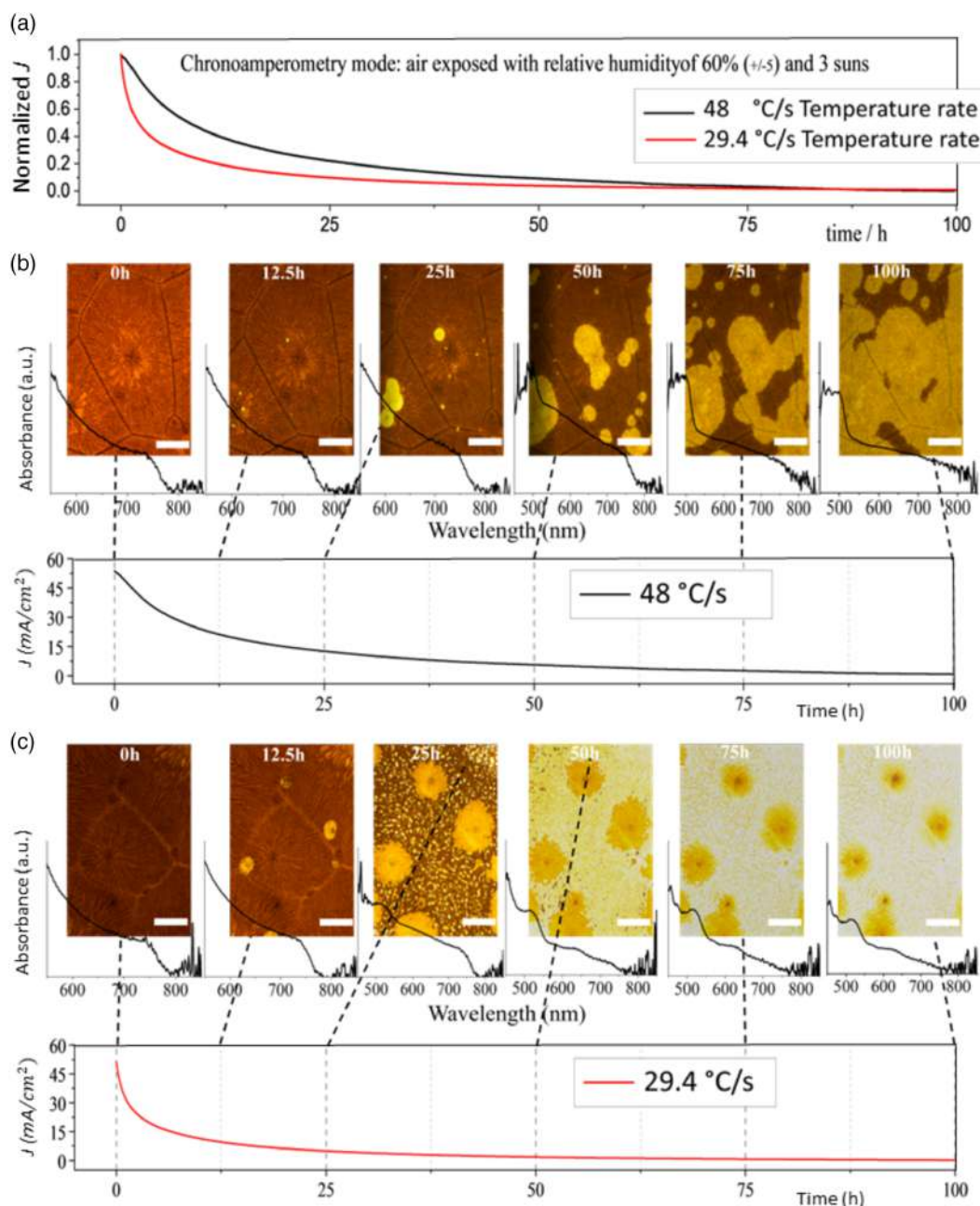

Figure 5. Degradation measurements under 60% RH and 3 sun illumination. a) Chronoamperometry of 100 h for 48 and $29.4\,°C\,s^{-1}$ heating rate samples. b) Chronoamperometry measurement showing the status of the surface at different times with the respective absorbance graph of sample for $48\,°C\,s^{-1}$ annealing. Scale bar is 100 μm. d) Chronoamperometry measurement showing the status of the surface at different moments with the respective absorbance graph of sample for $29.4\,°C\,s^{-1}$ heating rate. Scale bar is 50 μm.

capacitance, C_{dr}, in series with a resistive process, R_{dr}.[69] Measurements were performed at V_{oc} under different light intensities. This fact allowed obtaining the ideality factor, n, of both samples by two different measurements: 1) from the slope of V_{oc} versus light intensity[70,71] (see Figure 4b) and from the slope of R_{rec} versus V_{oc} (see Figure 4c).[70,72] Both approaches result in a good agreement in n values obtained, pointing to the consistency of the approach and of the equivalent circuit model employed (see Figure 4a). The ideality factor values indicate that the recombination mechanism of the two samples is different. Samples synthesized at $29\,°C\,s^{-1}$ present $n \approx 2$, pointing to a trap-mediated bulk recombination.[71] In contrast, samples prepared at $48\,°C\,s^{-1}$ show $n \approx 1.5$ indicating contributions from bulk and surface recombination, which is in line with the bulk defect reduction discussed above. In addition, higher recombination resistance of devices prepared at $48\,°C\,s^{-1}$ heating rate (see Figure 4b) also points to a lower recombination rate, indicating that the higher heating rate reduces bulk recombination, causing higher V_{oc}.[66–68] In addition, the higher influence of surface recombination could be the origin of the lower FF observed for these samples, despite the samples synthesized at $29\,°C\,s^{-1}$ heating rate have a higher series resistance, $4\,\Omega\,cm^2$, than the films synthesized at higher temperatures, $2\,\Omega\,cm^2$, which could be related with the quality of the materials and their greater resistance to electronic transport, mainly due to low homogeneity of the film and the presence of more defects.

Finally, to obtain information on device stability, the solar cells were stressed by measuring continuous chronoamperometry for 100 h at J_{sc} conditions, without encapsulation, at harsh measurement conditions, 3 sun illumination, and ambient atmosphere with 60% relative humidity (RH). Along with all measurements, surface image of the perovskite film of devices was recorded and absorbance at the observed area was measured. The obtained current over 100 h can be observed in **Figure 5**a. Again, the device made at $48\,°C\,s^{-1}$ heating rate presents a slower decay than the sample of $29.4\,°C\,s^{-1}$ rate.

Figure 5b,c, displays each curve with a snapshot of the surface image and optical absorbance along with the recorded measurement. At the beginning of the recorded measurement, pinholes-free grains, well-defined grain boundaries, and a larger size is observed for $48\,°C\,s^{-1}$ in comparison to $29.4\,°C\,s^{-1}$. At 12.5 h, the current value has decayed and spots of degradation that do not reduce absorbance intensity become clear. These first degraded microspots that appeared at 12.5 h start to extend degradation across the whole area as shown at 25 h for $29.4\,°C\,s^{-1}$, while for $48\,°C\,s^{-1}$ the degradation effect is lower and exhibits a more degraded area. At 50 h, the current has decreased almost 10 times, with a lower value for $29.4\,°C\,s^{-1}$ devices. The widely extended degradation causes a decrease of absorbance with a clear slope at around 500 nm, possibly related to the PbI_2 precursor,[73] while on the other side, the $48\,°C\,s^{-1}$ device still retains its portrait. The last two images, at 75 and 100 h, reveal a surface mostly degraded with negligible current and an absorbance that reflects only the presence of PbI_2[74,75] due to perovskite photodecomposition.

The path showed by the $48\,°C\,s^{-1}$ device indicates that degradation starts in over the grain, and then some spots appear next to the grain boundary. The different degradation paths followed by the films are linked to the morphological and structural results. The X-ray diffraction (XRD) measurement (see Figure S6,

Table 2. General statistical information of analyzed SEM images. Analyzed area: $1196.26 \times 897.20\,\mu m^2$.

Heating rate	$48\,°C\,s^{-1}$	$29.4\,°C\,s^{-1}$
Quantity of grains	337	458
Average area [μm^2]	5242	3683
Percentage of grains between 0 and $6000\,\mu m^2$	70.03	82.53

Supporting Information) exhibits the characteristic peaks at 12.7° of $PbI_2°$ and 14° of methylammonium iodide (MAI) that belong to the plane (110) of the tetragonal phase of the $MAPbI_3$. A better crystallinity as analyzed from the highest intensity of the characteristic peaks and a negligible presence of PbI_2 is observed for samples with the highest heating rate in comparison to a lower extracted crystallinity for $29.4\,°C\,s^{-1}$ samples. In addition, statistical analysis was performed based on SEM images (Figure S7a, Supporting Information) using an area of $1196.26 \times 897.20\,\mu m^2$ for each surface. The histogram obtained (see Figure S7b, Supporting Information) shows the presence of more grains of smaller area for $29.4\,°C\,s^{-1}$ in comparison to $48\,°C\,s^{-1}$ while this tendency changes for areas larger than $6000\,\mu m^2$. In accordance to this procedure (see Experimental Section), a total of 337 grains were obtained for $48\,°C\,s^{-1}$ and 458 grains for $29.4\,°C\,s^{-1}$ as shown in **Table 2**, corresponding to an average grain size of 5242 and $3683\,\mu m^{2.}$ respectively. There will thus be more grain boundaries for the films annealed at $29.4\,°C\,s^{-1}$ causing thinner borders and enhancing the possibility of higher amount of defects, while for $48\,°C\,s^{-1}$ any possible degradation through cavities is delayed, in agreement with PDS measurements[76] and stability performance. In fact, these microsegregated spots shown at the perovskite grain domains may be related to defects created during crystal growth, allowing further perovskite decomposition.[19,77–79]

3. Conclusions

Thin polycrystalline $MAPbI_3$ perovskite films were crystallized in rapid processing using the FIRA technique with heating rate control, resulting in large and compact grains with microsized domains. The screening through heating rates revealed the effects on film surface roughness, size, and crystallinity. Higher heating rates exhibit smoother film surfaces with homogenous topology, decreasing defect density and enhancing the electronic behavior as revealed by Raman, PL, and EIS spectroscopies, in turn beneficial for efficiency and stability of the final manufactured devices. The devices made with the higher heating rate ($48\,°C\,s^{-1}$) showed superior performance in comparison to devices made with films produced at lower heating rates ($29\,°C\,s^{-1}$). The champion device made of $MAPbI_3$ without mixed halides or multiple A-site cations showed a PCE of 19.5% and 18.4% in backward and forward scans (average PCE 18.95%), with the low hysteresis and the main loss in a decrease of the FF from 0.75 to 0.71. The degradation behavior was reported and we observed segregated microspots, from which degradation begins and expands across the surface. The most efficient devices were manufactured with the highest

heating rate processed perovskite films. These champion solar cells slowed down the degradation process due to improved crystal film growth. Higher performances and stabilities were observed for higher heating rates, with the added benefit of a lower process time, ultimately very important for the implementation of FIRA technology for the industrial development of perovskite solar cells.

4. Experimental Section

Materials: All materials were reagent grade and were used as received: zinc powder (99.995%) and hydrochloric acid (HCl 37%) are from Aldrich, and fluorine tin oxide (FTO)-coated glass from Pilkington NSG TEC. To fabricate the electron transporting layer titanium diisopropoxide bis(acetylacetonate) from Merck (75 wt% in isopropanol and TiO_2 paste (Dyesol 30 NR-D) were used. Perovskite precursors are lead iodide (PbI_2, >98%, from Aldrich) and MAI (98%, from Greatcellsolar). Precursors for hole transporting layer are lithium bis(trifluoromethylsulfonyl)imide (Li-TFSI, 99.95%, from Sigma-Aldrich) and 2,20,7,70-tetrakis[*N,N*-di(4-methoxyphenyl) amino]-9,90-spirobifluorene (spiro-OMeTAD 99%, from Merck). The solvents used are 2-propanol (99.7%), ethanol (96%), and acetone (99.25%) from PanReac; dimethyl formamide (DMF anhydrous 99.9%), dimethyl sulfoxide (DMSO anhydrous 99.9%), clorobenzene (CB anhydrous 99.8%), acetonitrile (MeCN anhydrous 99.8%), 4-*tert*-butylpiridine (TBP 96%) from sigma-Aldrich); and tris(2-(1H-pyrazol-1-yl)-4-*tert*-butylpyridine)-cobalt(III)tris(bis(trifluoromethylsulfonyl)imide) (FK209, Dynamo).

Device Fabrication: FTO glasses were etched by placing zinc powder on an area of the glass and dropped HCl solution of 2 M on it. After 2 min, the excess of zinc was removed with distilled water and cleaned with a solution of Hellmanex. Then three consecutive sonications of 15 min were made in the following order: Hellmanex solution, acetone, and ethanol. At the end, the substrates were dried using a flow of air. Before the deposition of the layer the substrates were submitted to a UV treatment for 15 min and then substrates were covered on opposite side of the etched part by metal bars and heated up to 450 °C. Once the substrates remain 10 min at the settled temperature it was sprayed a solution of 0.4 mL of acetylacetonate, 0.6 mL of titanium diisopropoxide bis(acetylacetonate) stock solution (75 wt% in isopropanol), and 9 mL of absolute ethanol. After that the substrates stayed 10 min at the mentioned temperature and waited for them to cool down below 150 °C. Over the area covered by the bars it was put tape and then it was deposited by spin coating at 4000 RPM for 10 s 50 µL of a solution composed by TiO_2 paste 30-NRD in ethanol (1:5 weight ratio). After that samples were dried at 100 °C for 10 min and then heated up to 500 °C for 30 min. Once samples cooled down up to room temperature they were moved to glove box for perovskite deposition. Perovskite solution was prepared by using 4:1 (DMF:DMSO volume ratio) as solvent. At first it was weighted MAI and once it was dissolved it was added PbI2 and heated up to 70 °C to dissolve all the precursors that result in a solution of 1.4 M concentration. Then 50 µL of solution was deposited by spin coating at 4000 RPM for 10 s and moved inside FIRA to anneal them for the selected time (see Figure S8, Supporting Information, for a picture of the FIRA experimental setup). Hole transporting layer was made by mixing 70 mM of spiro in chlorobenzene and added to it 1.8 M solution of Li-TFSI in acetonitrile, 4-*tert*-butylpiridine in acetonitrile at 3.3 molar concentration in respective to spiro and 0.25 M solution of FK209. Then the solution was spin-coated at 4000 RPM for 10 s over the perovskite. Finally, samples were scratched on the opposite side of etched side and then 80 nm of Au was deposited by thermal evaporation.

SEM: SEM was performed by the equipment JEOL 3100F equipped with an electron gun employing 5 kV which allow us to magnifications from 5000× up to 25 000× to analyze surface. ImageJ was utilized to adjust contrast of images and identify the borders of the grains observed by SEM. Then, utilizing the threshold of each image it was possible to obtain the areas of the grains employing a plugin to measure the surrounded grains.

XRD: The XRD profiles were registered by a diffractometer (Bruker AXS, D8 Advance) equipped with a primary monochromator of Ge. Measurements were taken using Cu Kα radiation (wavelength of $l = 1.5406$ A) over a 2θ range between 5° and 70° with a step size of 0.02°.

AFM: AFM images were taken using tapping mode with capacity to analyze surface of 20 µm² with maximum high of 3µm using JSPM-5200 JEOL Scanning probe.

Optical Characterization: UV–vis absorption of the thin films was characterized using a UV–vis absorption spectrophotometer (Varian, Cary 300) in the wavelength range of 400–850 nm.

Steady-State PL Emission: PL of the films was carried out using the 514 nm excitation wavelength coupled with a CCD detector (InGaAsAndor-iDUS DU490A-2.2) with an adaptive focus imaging spectrograph (Kymera KY-193i-B2). A commercial continuous laser (532 nm, GL532RM-150) was used as an excitation source.

CM: CM of films was employed by using an optic profilometer Model PLm2300 from Sensofar utilizing an excitation wavelength of 514 nm. Optical transmission measurements were performed using a Zeiss Axio-Scope A1 Pol using a Zeiss EC Epiplan-Apochromat 10×, 50× objectives and a xenon light source (Ocean Optics HPX-2000). For spectroscopic measurements, an optical fiber (QP230-2-XSR, 230 µm core) collected the transmitted light from the sample. The spectra were recorded by a spectrometer (Ocean Optics Maya2000 Pro). All spectra were obtained at room temperature in transmission.

Raman Spectroscopy (RE): RE was performed on a Renishaw InVia spectrometer using a frequency doubled Nd:YAG laser operating at 532 nm with a grating, slit, and spectral length to enable $<0.5 \text{ cm}^{-1}$ resolution per pixel in the CCD. The spectrometer was calibrated with the signifying peak in Si to $520.5 \pm 0.2 \text{ cm}^{-1}$ and low laser intensities were utilized to ensure that no laser heating effects were present.

Current–Voltage (J–V) measurement: Photovoltaic parameters for unencapsulated n–i–p devices were obtained using VeraSol LED solar simulator (Newport) which gives an AM1.5G (100 mW cm⁻²) light illumination conditions coupled with a Keithley 2604 sourcemeter to measure current–voltage. Each measured was taken with Tracer software and done at ambient conditions ($T = 25$ °C, RH ≈ 40%) using a scan rate of 10 mV s⁻¹ and a shadow mask of 0.16 cm². The stability measurements of devices were performed under 1 sun illumination in a sealed holder with nitrogen flow at M_{pp}. Every 10 min a J–V was measured to track the M_{pp} of the device.

IPCE: IPCE measurements were performed using a Xenon lamp with a monochromator Oriel Cornestone 130 which was used to measure along the wavelength of the spectrum. Prior measurement, calibration was done using a reference photodiode of silicon and each measurement was obtained using TRACQ BASIC software. Finally, EQE scans were taken from 300 to 810 nm in steps of 10 nm.

Chronoamperometry: Chronoamperometry data were obtained by a Potentiostat Autolab PGSTAT30 employing 3 sun illumination over devices at ambient conditions of 60% RH measuring at 0 V for 100 h.

EIS: The EIS was measured by using a Potentiostat Autolab PGSTAT30 employing different filters to change light intensity up to 1 sun. For each voltage point (V_{OC}), EIS was measured with an AC 10 mV voltage perturbation from 1 MHz to 100 mHz. Nova software was used to generate data and Z-View software for modeling the equivalent circuit model used to fit the spectra, respectively.

Supporting Information

Supporting Information is available from the Wiley Online Library or from the author.

Acknowledgements

Conflict of Interest

The authors declare no conflict of interest.

Data Availability Statement

The data that support the findings of this study are available from the corresponding author upon reasonable request.

Keywords

crystal growth, defects, flash infrared annealing, perovskites, processing, stability

[1] A. Kojima, K. Teshima, Y. Shirai, T. Miyasaka, *J. Am. Chem. Soc.* **2009**, *131*, 6050.

[2] H. Singh, P. Dey, S. Chatterjee, P. Sen, T. Maiti, *Sol. Energy* **2021**, *220*, 258.

[3] M. I. H. Ansari, A. Qurashi, M. K. Nazeeruddin, *J. Photochem. Photobiol., C* **2018**, *35*, 1.

[4] P. K. Nayak, S. Mahesh, H. J. Snaith, D. Cahen, *Nat. Rev. Mater.* **2019**, *4*, 269.

[5] W.-J. Yin, J.-H. Yang, J. Kang, Y. Yan, S.-H. Wei, *J. Mater. Chem. A* **2015**, *3*, 8926.

[6] R. Vidal, J.-A. Alberola-Borràs, N. Sánchez-Pantoja, I. Mora-Seró, *Adv. Energy Sustainability Res.* **2021**, *2*, 2000088.

[7] N. K. Tailor, M. Abdi-Jalebi, V. Gupta, H. Hu, M. I. Dar, G. Li, S. Satapathi, *J. Mater. Chem. A* **2020**, *8*, 21356.

[8] K. Liao, C. Li, L. Xie, Y. Yuan, S. Wang, Z. Cao, L. Ding, F. Hao, *Nano-Micro Lett.* **2020**, *12*, 156.

[9] M. A. Haque, J. Troughton, D. Baran, *Adv. Mater.* **2020**, *10*, 1902762.

[10] M. Abbas, L. Zeng, F. Guo, M. Rauf, X. C. Yuan, B. Cai, *Materials* **2020**, *13*, 4851.

[11] C. Liu, Y.-B. Cheng, Z. Ge, *Chem. Soc. Rev.* **2020**, *49*, 1653.

[12] H. Shahivandi, M. Vaezzadeh, M. Saeidi, *Sol. Energy Mater. Sol. Cells* **2020**, *208*, 110383.

[13] M. I. Asghar, J. Zhang, H. Wang, P. D. Lund, *Renewable Sustainable Energy Rev.* **2017**, *77*, 131.

[14] W. Peng, B. Anand, L. Liu, S. Sampat, B. E. Bearden, A. V. Malko, Y. J. Chabal, *Nanoscale* **2016**, *8*, 1627.

[15] G. Han, T. M. Koh, S. S. Lim, T. W. Goh, X. Guo, S. W. Leow, R. Begum, T. C. Sum, N. Mathews, S. Mhaisalkar, *ACS Appl. Mater. Interfaces* **2017**, *9*, 21292.

[16] J. Xue, R. Wang, Y. Yang, *Nat. Rev. Mater.* **2020**, *5*, 809.

[17] A.-F. Castro-Méndez, J. Hidalgo, J.-P. Correa-Baena, *Adv. Mater.* **2019**, *9*, 1901489.

[18] Y. Chen, H. Zhou, *J. Appl. Phys.* **2020**, *128*, 060903.

[19] F. Wang, S. Bai, W. Tress, A. Hagfeldt, F. Gao, *npj Flexible Electron.* **2018**, *2*, 22.

[20] N. Ahn, K. Kwak, M. S. Jang, H. Yoon, B. Y. Lee, J.-K. Lee, P. V. Pikhitsa, J. Byun, M. Choi, *Nat. Commun.* **2016**, *7*, 13422.

[21] J. S. Yun, J. Kim, T. Young, R. J. Patterson, D. Kim, J. Seidel, S. Lim, M. A. Green, S. Huang, A. Ho-Baillie, *Adv. Funct. Mater.* **2018**, *28*, 1705363.

[22] M. Hada, M. Abdullah Al Asad, M. Misawa, Y. Hasegawa, R. Nagaoka, H. Suzuki, R. Mishima, H. Ota, T. Nishikawa, Y. Yamashita, Y. Hayashi, K. Tsuruta, *Appl. Phys. Lett.* **2020**, *117*, 253304.

[23] Y. Shao, Y. Fang, T. Li, Q. Wang, Q. Dong, Y. Deng, Y. Yuan, H. Wei, M. Wang, A. Gruverman, J. Shield, J. Huang, *Energy Environ. Sci.* **2016**, *9*, 1752.

[24] H. Khassaf, S. K. Yadavalli, Y. Zhou, N. P. Padture, A. I. Kingon, *J. Phys. Chem. C* **2019**, *123*, 5321.

[25] M. Xiao, F. Huang, W. Huang, Y. Dkhissi, Y. Zhu, J. Etheridge, A. Gray-Weale, U. Bach, Y. B. Cheng, L. Spiccia, *Angew. Chem., Int. Ed.* **2014**, *53*, 9898.

[26] Y. Zhou, M. Yang, W. Wu, A. L. Vasiliev, K. Zhu, N. P. Padture, *J. Mater. Chem. A* **2015**, *3*, 8178.

[27] N. J. Jeon, J. H. Noh, Y. C. Kim, W. S. Yang, S. Ryu, S. I. Seok, *Nat. Mater.* **2014**, *13*, 897.

[28] J.-P. Correa-Baena, W. Tress, K. Domanski, E. H. Anaraki, S.-H. Turren-Cruz, B. Roose, P. P. Boix, M. Grätzel, M. Saliba, A. Abate, A. Hagfeldt, *Energy Environ. Sci.* **2017**, *10*, 1207.

[29] Z. Chu, M. Yang, P. Schulz, D. Wu, X. Ma, E. Seifert, L. Sun, X. Li, K. Zhu, K. Lai, *Nat. Commun.* **2017**, *8*, 2230.

[30] N. Sakai, Z. Wang, V. M. Burlakov, J. Lim, D. McMeekin, S. Pathak, H. J. Snaith, *Small* **2017**, *13*, 1602808.

[31] L. Gao, G. Yang, *Sol. RRL* **2020**, *4*, 1900200.

[32] S. Sanchez, U. Steiner, X. Hua, *Chem. Mater.* **2019**, *31*, 3498.

[33] S. Ghosh, S. Mishra, T. Singh, *Adv. Mater. Interfaces* **2020**, *7*, 2000950.

[34] L. Zeng, S. Chen, K. Forberich, C. J. Brabec, Y. Mai, F. Guo, *Energy Environ. Sci.* **2020**, *13*, 4666.

[35] S. T. Williams, A. Rajagopal, C.-C. Chueh, A. K. Y. Jen, *J. Phys. Chem. Lett.* **2016**, *7*, 811.

[36] P. S. V. Ling, A. Hagfeldt, S. Sanchez, *JoVE* **2021**, *168*, e61730.

[37] S. Sanchez, X. Hua, N. Phung, U. Steiner, A. Abate, *Adv. Mater.* **2018**, *8*, 1702915.

[38] S. Sanchez, N. Christoph, B. Grobety, N. Phung, U. Steiner, M. Saliba, A. Abate, *Adv. Mater.* **2018**, *8*, 1802060.

[39] S. Sánchez, J. Jerónimo-Rendon, M. Saliba, A. Hagfeldt, *Mater. Today* **2020**, *35*, 9.

[40] S. Sánchez, M. Vallés-Pelarda, J.-A. Alberola-Borràs, R. Vidal, J. J. Jerónimo-Rendón, M. Saliba, P. P. Boix, I. Mora-Seró, *Mater. Today* **2019**, *31*, 39.

[41] S. Sánchez, X. Hua, A. Günzler, E. Bermúdez-Ureña, D. Septiadi, M. Saliba, U. Steiner, *Cryst. Growth Des.* **2020**, *20*, 670.

[42] S. Sánchez, L. Pfeifer, N. Vlachopoulos, A. Hagfeldt, *Chem. Soc. Rev.* **2021**, *50*, 7108.

[43] C. Eames, J. M. Frost, P. R. F. Barnes, B. C. O'Regan, A. Walsh, M. S. Islam, *Nat. Commun.* **2015**, *6*, 7497.

[44] A. M. A. Leguy, P. Azarhoosh, M. I. Alonso, M. Campoy-Quiles, O. J. Weber, J. Yao, D. Bryant, M. T. Weller, J. Nelson, A. Walsh, M. van Schilfgaarde, P. R. F. Barnes, *Nanoscale* **2016**, *8*, 6317.

[45] X. Zhang, J.-X. Shen, W. Wang, C. G. Van de Walle, *ACS Energy Lett.* **2018**, *3*, 2329.

[46] Z. Shi, A. H. Jayatissa, *Materials* **2018**, *11*, 729.

[47] S. Pratap, F. Babbe, N. S. Barchi, Z. Yuan, T. Luong, Z. Haber, T.-B. Song, J. L. Slack, C. V. Stan, N. Tamura, C. M. Sutter-Fella, P. Müller-Buschbaum, *Nat. Commun.* **2021**, *12*, 5624.

[48] T. W. Kim, N. Shibayama, L. Cojocaru, S. Uchida, T. Kondo, H. Segawa, *Adv. Funct. Mater.* **2018**, *28*, 1804039.

[49] L.-C. Chen, C.-C. Chen, J.-C. Chen, C.-G. Wu, *Sol. Energy* **2015**, *122*, 1047.

[50] S. Sánchez, S. Cacovich, G. Vidon, J. F. Guillemoles, F. T. Eickemeyer, S. M. Zakeeruddin, J. Schawe, J. F. Löffler, C. Cayron, P. Schouwink, M. Grätzel, *Energy Environ. Sci.* **2022**, *15*, 3862.

[51] A. Dualeh, N. Tétreault, T. Moehl, P. Gao, M. K. Nazeeruddin, M. Grätzel, *Adv. Funct. Mater.* **2014**, *24*, 3250.

[52] Y. Jiang, L. Pan, D. Wei, W. Li, S. Li, S.-E. Yang, Z. Shi, H. Guo, T. Xia, J. Zang, Y. Chen, *Sol. Energy* **2018**, *174*, 218.

[53] H. Zhang, Y. Wang, H. Wang, M. Ma, S. Dong, Q. Xu, *J. Alloys Compd.* **2019**, *773*, 511.

[54] S. Sánchez, B. Carlsen, V. Škorjanc, N. Flores, P. Serafini, I. Mora-Seró, P. Schouwink, S. M. Zakeeruddin, M. Graetzel, A. Hagfeldt, *J. Mater. Chem. A* **2021**, *9*, 26885.

[55] T. Haeger, R. Heiderhoff, T. Riedl, *J. Mater. Chem. C* **2020**, *8*, 14289.

[56] R. Heiderhoff, T. Haeger, N. Pourdavoud, T. Hu, M. Al-Khafaji, A. Mayer, Y. Chen, H.-C. Scheer, T. Riedl, *J. Phys. Chem. C* **2017**, *121*, 28306.

[57] X. Qian, X. Gu, R. Yang, *Appl. Phys. Lett.* **2016**, *108*, 063902.

[58] N. Cho, F. Li, B. Turedi, L. Sinatra, S. P. Sarmah, M. R. Parida, M. I. Saidaminov, B. Murali, V. M. Burlakov, A. Goriely, O. F. Mohammed, T. Wu, O. M. Bakr, *Nat. Commun.* **2016**, *7*, 13407.

[59] K. Nakada, Y. Matsumoto, Y. Shimoi, K. Yamada, Y. Furukawa, *Molecules* **2019**, *24*, 626.

[60] M. Ledinský, P. Löper, B. Niesen, J. Holovský, S.-J. Moon, J.-H. Yum, S. De Wolf, A. Fejfar, C. Ballif, *J. Phys. Chem. Lett.* **2015**, *6*, 401.

[61] A. M. A. Leguy, A. R. Goñi, J. M. Frost, J. Skelton, F. Brivio, X. Rodríguez-Martínez, O. J. Weber, A. Pallipurath, M. I. Alonso, M. Campoy-Quiles, M. T. Weller, J. Nelson, A. Walsh, P. R. F. Barnes, *Phys. Chem. Chem. Phys.* **2016**, *18*, 27051.

[62] M. A. Pérez-Osorio, Q. Lin, R. T. Phillips, R. L. Milot, L. M. Herz, M. B. Johnston, F. Giustino, *J. Phys. Chem. C* **2018**, *122*, 21703.

[63] J. Ibaceta-Jaña, R. Muydinov, P. Rosado, H. Mirhosseini, M. Chugh, O. Nazarenko, D. N. Dirin, D. Heinrich, M. R. Wagner, T. D. Kühne, B. Szyszka, M. V. Kovalenko, A. Hoffmann, *Phys. Chem. Chem. Phys.* **2020**, *22*, 5604.

[64] A. D. Wright, R. L. Milot, G. E. Eperon, H. J. Snaith, M. B. Johnston, L. M. Herz, *Adv. Funct. Mater.* **2017**, *27*, 1700860.

[65] M. Ledinsky, T. Schönfeldová, J. Holovský, E. Aydin, Z. Hájková, L. Landová, N. Neyková, A. Fejfar, S. De Wolf, *J. Phys. Chem. Lett.* **2019**, *10*, 1368.

[66] L.-C. Chen, K.-L. Lee, W.-T. Wu, C.-F. Hsu, Z.-L. Tseng, X. H. Sun, Y.-T. Kao, *Nanoscale Res. Lett.* **2018**, *13*, 140.

[67] H. D. Kim, H. Ohkita, H. Benten, S. Ito, *Adv. Mater.* **2016**, *28*, 917.

[68] X. Ren, Z. Yang, D. Yang, X. Zhang, D. Cui, Y. Liu, Q. Wei, H. Fan, S. Liu, *Nanoscale* **2016**, *8*, 3816.

[69] S.-M. Yoo, S. J. Yoon, J. A. Anta, H. J. Lee, P. P. Boix, I. Mora-Seró, *Joule* **2019**, *3*, 2535.

[70] E. Velilla, F. Jaramillo, I. Mora-Seró, *Nat. Energy* **2021**, *6*, 54.

[71] W. Tress, M. Yavari, K. Domanski, P. Yadav, B. Niesen, J. P. Correa Baena, A. Hagfeldt, M. Graetzel, *Energy Environ. Sci.* **2018**, *11*, 151.

[72] L. Cont, reras-Bernal, S. Ramos-Terrón, A. Riquelme, P. P. Boix, J. Idígoras, I. Mora-Seró, J. A. Anta, *J. Mater. Chem. A* **2019**, *7*, 12191.

[73] S. M. Jain, B. Philippe, E. M. J. Johansson, B.-W. Park, H. Rensmo, T. Edvinsson, G. Boschloo, *J. Mater. Chem. A* **2016**, *4*, 2630.

[74] P. Basumatary, P. Agarwal, *J. Mater. Sci.: Mater. Electron.* **2020**, *31*, 10047.

[75] M. Shahiduzzaman, K. Hamada, K. Yamamoto, M. Nakano, M. Karakawa, K. Takahashi, T. Taima, *Cryst. Growth Des.* **2019**, *19*, 5320.

[76] T.-X. Qin, E.-M. You, M.-X. Zhang, P. Zheng, X.-F. Huang, S.-Y. Ding, B.-W. Mao, Z.-Q. Tian, *Light Sci. Appl.* **2021**, *10*, 84.

[77] J. A. McLeod, L. Liu, *J. Phys. Chem. Lett.* **2018**, *9*, 2411.

[78] T. Wang, G. Lian, L. Huang, F. Zhu, D. Cui, Q. Wang, Q. Meng, C.-P. Wong, *ACS Appl. Mater. Interfaces* **2020**, *12*, 38314.

[79] Y. Wang, W.-H. Fang, R. Long, O. V. Prezhdo, *J. Phys. Chem. Lett.* **2019**, *10*, 1617.